



University
of Glasgow

Bobyanko, J., MacLaren, I., and Craven, A. J. (2015) Spectrum imaging of complex nanostructures using DualEELS: I. digital extraction replicas. *Ultramicroscopy*, 149. pp. 9-20.

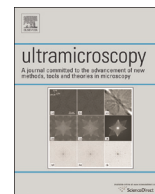
Copyright © 2014 The Authors.

This work is made available under the Creative Commons Attribution – NonCommercial-NoDerivatives 3.0 License (CC BY-NC-ND 3.0)

Version: Published

<http://eprints.gla.ac.uk/99265/>

Deposited on: 11 November 2014



Spectrum imaging of complex nanostructures using DualEELS: I. digital extraction replicas



Joanna Bobynko, Ian MacLaren*, Alan J. Craven

SUPA School of Physics and Astronomy, University of Glasgow, Glasgow G12 8QQ, UK

ARTICLE INFO

Article history:

Received 8 August 2014

Received in revised form

16 October 2014

Accepted 26 October 2014

Available online 4 November 2014

ABSTRACT

This paper shows how it is possible to use Dual Electron Energy Loss Spectroscopy (DualEELS) to digitally extract spectrum images for one phase of interest in a complex nanostructured specimen. The specific cases studied here concern Nb or V precipitates, a few nanometres in size, in high manganese steels. The procedures outlined allow the extraction of the precipitate signal from the Fe–Mn matrix, as well as correction for surface oxide and any surface carbon contamination. The resulting precipitate-only spectrum images are then suitable for quantitative analysis of the precipitate chemistry. This procedure results in much improved background shapes under all edges of interest, mainly as a result of the removal of the extended electron loss fine structure (EXELFS) from the elements in the matrix. This allows the reliable extraction of even tiny quantities of elements, such as low levels of nitrogen in some carbide precipitates. As well as being relevant to precipitation in steels, these techniques will be widely applicable to the separation of chemically-distinct phases in complex nanostructured samples, and can be viewed as a digital version of the extraction replica technique.

© 2014 The Authors. Published by Elsevier B.V. This is an open access article under the CC BY-NC-ND license (<http://creativecommons.org/licenses/by-nc-nd/3.0/>).

1. Introduction

An important class of analytical problems is the study of small particles in a matrix where information on both the particles and the inter-relationships between the particle and the matrix are important. For instance, nanoscale precipitates are widely used for dispersion hardening of metallic alloys, nanoparticle catalysts are often hosted in complex, three-dimensional supports, and many functional polymers are complex blends of different components. Understanding the local composition, chemistry, size, morphology, and number or volume density are key issues. One key step to achieving this is separating the signals from different nanosized features. In view of the richness of information contained in electron energy loss spectroscopy (EELS) datasets, it is particularly worthwhile to find methodologies for performing this using EELS spectrum images.

The problem is simplified significantly if the particle contains a negligible amount of a key element in the matrix. In such situations, it is possible to separate the contributions from the matrix and the particle in a relatively straightforward way. This situation occurs in a number of metallurgical systems but is also found in supported catalyst systems.

This paper is concerned with the analysis of transition metal carbides (or carbonitrides), a few nanometres in size, in a high-

manganese steel. Such high manganese steels are currently under investigation as potential high strength, high ductility materials that will provide light, structural members with significant energy absorption in a crash situation. This would allow automotive manufacturers to combine improved fuel efficiency and improved passenger safety. The high manganese steels of interest fall into the category of a twinning-induced plasticity (TWIP) steels. Such steels are austenitic at room temperature and hence their ductility is far higher than the ferritic high strength low alloys (HSLA) steels currently used in the automotive industry. Their ultimate tensile strength is high and so, combined with the high ductility, deformation results in high energy absorption. One current difficulty, however, is that the yield strength of standard high-Mn steels is relatively low. To increase this to an acceptable level, precipitation (or dispersion) hardening is being investigated. In precipitation hardening, a high number density of small, “hard” particles is used to impede dislocation movement and hence increase the yield strength. Here, precipitation of V(C,N) or Nb(C,N) is being investigated as part of an EU-funded project (Research Fund for Coal and Steel–Precipitation in High Manganese Steels [PrecHiMn]).

A common approach to the analysis of precipitates is the use of extraction replicas [1,2]. This approach has the advantage that the matrix is totally removed allowing the size of the precipitates to be measured and their compositions analysed without interference from the matrix. However, all relationships with the matrix are lost and it is not possible to get the absolute number of precipitates per unit volume or the absolute volume fraction.

* Corresponding author.



University
of Glasgow

Bobyanko, J., MacLaren, I., and Craven, A. J. (2015) Spectrum imaging of complex nanostructures using DualEELS: I. digital extraction replicas. *Ultramicroscopy*, 149. pp. 9-20.

Copyright © 2014 The Authors.

This work is made available under the Creative Commons Attribution – NonCommercial-NoDerivatives 3.0 License (CC BY-NC-ND 3.0)

Version: Published

<http://eprints.gla.ac.uk/99265/>

Deposited on: 11 November 2014

Moreover, there is uncertainty about whether the smallest precipitates are extracted efficiently (or at all), about whether the etching process changes the precipitates, and about how well the distribution of precipitates in the matrix is transferred to the replica [3]. However, this technique is well-established, and relatively straightforward, and can cover relatively large areas of material with dimensions up to millimetres [1,2]. Experimental results on the high manganese steels investigated in the PrecHiMn project using extraction replicas show negligible Fe or Mn in the precipitates (unpublished work) and this is backed up from thermodynamic data [4].

Another powerful approach is the three-dimensional atom probe (3-DAP) [3,5]. It can reconstruct a large fraction of the atom positions in a sample and allow them to be mapped. It is sensitive to low concentrations of components. The absolute number per unit volume, the volume fraction and the size distribution can be measured. However, the analysis is limited to the volume of the needle shaped specimen used, determination of precipitate-matrix boundaries is non-trivial, trajectory aberrations and surface rearrangements can displace reconstructed atoms positions from their true ones and desorption of clusters complicates interpretation of atom positions. Determining the inter-relationships between the matrix and the precipitate is also challenging if not impossible. A key problem with small precipitates is that trajectory aberrations cause matrix atoms to appear within the precipitate. If it is known that there are no matrix elements in the precipitate, it is possible to correct for this effect [3].

The approach used in the current work builds on earlier work using electron energy loss spectroscopy (EELS) and scanning transmission electron microscopy (STEM) to perform spectrum imaging (SI) [3,6]. All the contrast mechanisms and signals in both conventional electron microscopy (CTEM) and STEM can be used to characterise the material. This allows a relatively large area of sample to be examined and chosen regions to be analysed in detail.

A modern probe corrected STEM with an electron spectroscopy system with DualEELS capability is essential to this work. Dual EELS allows the recording of both the low loss and core loss regions of the EELS spectrum at a pixel before moving on to the next pixel [7,8]. To deal with the large difference of signal intensity in the two regions, the low loss region is recorded with a short dwell time and the core loss region with a much longer dwell time and there is a well-defined ratio between the two times so that, in principle, the intensities of the two regions can be scaled to the same incident charge. This paper seeks to exploit the benefits provided by DualEELS acquisition.

The EELS spectrum provides a wealth of key information about the sample. The low loss region of the spectrum gives the thickness of the specimen, t , in terms of the inelastic mean free path, λ . If λ is known, t is known [9,10]. The energy thresholds of the ionisation edges identify the atoms present at a given pixel in the spectrum image. The intensity of an edge above the background is proportional to the amount of the element present and, when normalised by the low-loss intensity and a cross-section, it gives the absolute number of atoms per unit area. If the sample is homogeneous with a known crystal structure, the number of atoms per unit area can also be converted into a local thickness giving a cross-check on that obtained from the low loss. The energy loss near edge structure (ELNES) on the ionisation edge gives information about the local atomic environment and bonding.

If at least one major element in the matrix is not present in the particle, the contribution to the EELS spectrum from the matrix can be subtracted off. This is performed by scaling a spectrum from an area where there is only matrix and subtracting it from the spectrum at each pixel in a way that leaves no contribution from the matrix-specific element [3]. Essentially this is the digital

equivalent of the extraction replica technique. The same quantification processes outlined above can then be applied to the spectral data from the precipitate alone to give its composition, to determine its local thickness and to map the elemental distributions within it. This approach provides the volume of the precipitate and its pseudo three-dimensional shape. If a large enough area of specimen is mapped, the number density, volume fraction and the size distribution of the precipitates can be estimated [3].

This approach is sound in principle but there are a number of practical issues to be overcome to achieve the desired outcome. This paper describes these issues and shows how to deal with them in order to extract reliable signal intensities from the as-recorded data. A subsequent paper will deal with how to convert the extracted intensities into absolute values such as thickness and number of atoms per unit volume.

Before going into details, an outline of the issues and their sources is given. The issues arise from three principal sources, the instrumentation, the sample and the noise in the data. Each source contributes several issues and they need to be addressed at the most appropriate point in the processing procedure and this may differ from dataset to dataset.

In terms of the instrumentation, there are several challenges. Instabilities and drift in both the accelerating voltage and the spectrometer magnet current cause shifts of the position of the spectrum on the CCD detector. A high-energy x-ray or cosmic ray can excite the scintillator, causing a very high signal in one or a small number of adjacent pixels of the CCD detector. This is known as an “x-ray spike”. The ends of the spectrum can suffer a loss of collection efficiency due to shadowing effects caused by material at the edge of the beam path in the spectrometer. In the DualEELS system, there can be “bleed-through” between the core-loss spectrum and the low loss spectrum due to multiple back-scattering of electrons within the spectrometer detector chamber. This results in a spurious background under the low loss spectrum. At the relatively low spectrometer dispersions used in this work, there is a non-linearity in the dispersion of the spectrometer.

The sample issues arise from the differences between the ideal sample, where only matrix and precipitate are present, and the real sample, where the matrix has a uniform, thin layer of epitaxial Fe_3O_4 on its surface, superimposed on which there may be a layer of amorphous carbon of variable thickness. These ideal and real cases are shown schematically in Fig. 1a and b respectively. For simplicity, the surface layers are shown on one side only. In the ideal case, when the matrix spectrum is scaled and subtracted, the only material from which information comes is the precipitate itself, as shown schematically in Fig. 1c. In the real case, when the matrix spectrum is scaled and subtracted from a pixel with only signal from the matrix, essentially the entire oxide signal is removed. However, since the thickness of the amorphous carbon is non-uniform, the residual signal from it will vary from pixel to pixel. In the case where the matrix signal is scaled and subtracted from a pixel where there is also signal from the precipitate, only a fraction of the oxide signal is removed and again there will be a variable amount signal from amorphous carbon. Fig. 1d shows schematically the material from which information comes after removal of the matrix contribution in a real sample. Correction for these residual surface contributions is made at the end of the processing procedure.

Noise in the data is always an issue in spectrum imaging because of the limited dynamic range of the EELS detector and the limited dwell time imposed on spectrum image acquisition by system stability and/or operator patience. Principal component analysis (PCA) is a statistical method that separates out the information present into a number of components. A limited number of components carry most of the information while the rest contain only noise. Unfortunately, the information contained in

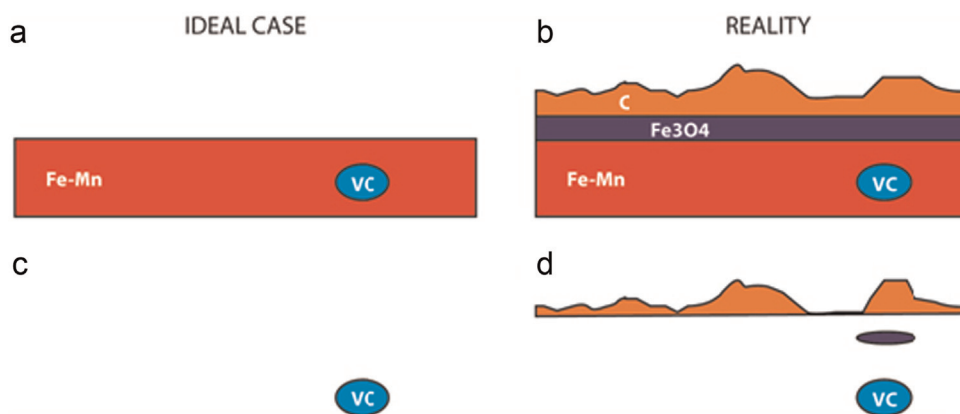


Fig. 1. Schematic diagrams of the ideal (a) and real (b) samples with the contributing material left after removal of the matrix in the ideal (c) and real (d) cases. All the Fe_3O_4 and amorphous carbon are shown on one surface for clarity.

the individual components is not easily interpretable in physical terms. However, the data can be reconstructed using only the information-containing components, thus reducing the noise [11]. Care has to be taken not to introduce additional artefacts by excluding components which actually contain significant information. In principle, PCA should be applied to the as-recorded data. In practice, the artefacts in the data then appear as information spread over a wide range of components. Here, a pragmatic approach is taken in that PCA is applied at the most effective point in the processing procedure.

While PCA significantly reduces the noise in the data, the limited dynamic range of the CCD still results there being very significant noise at the high-energy end of the low loss region where the recorded signal is rather low. Thus the splicing procedure introduces “noise” into the scaling factor. In many situations, there is no information in the part of the low loss region adjacent to the splice point. Thus the noise can be averaged by fitting a power law function to the data in this region and then replacing the data by the fitted function. In this way, the “noise” in the scaling factor is significantly reduced.

Once the splicing has been successfully carried out, it is then possible to deconvolve the effects of multiple scattering from the spectrum image using the Fourier-log method [12]. At this point, it is possible to estimate and subtract the matrix contribution from the deconvolved spectrum image, producing a final digitally extracted SI from just the precipitate. Corrections to remove amorphous carbon and surface oxide from the signal may also be required as outlined above.

This paper describes in detail a procedure for performing the steps outlined above and its application to carbides in V- and Nb-microalloyed high Mn steels. It is shown that it is possible to produce extracted spectrum images suitable for quantitative analysis. The further quantitative analysis of the resulting spectrum images will be described in part II of the paper.

2. Experimental methods

2.1. Materials and sample preparation

The material investigated consists of two steels based on the same Fe–Mn base alloy, whose composition in weight per cent is 20%Mn, 1.5%Al, 0.6%C with the balance being Fe. One of the steels has a 0.2% addition of V and the other a 0.1% addition of Nb in order to form carbides for dispersion hardening. Below, these are referred to as the V steel and the Nb steel respectively. Both steels have a small and undetermined Ti content in the range 60–70 ppm

from the original feedstock. Similar processing schedules were applied to both steels with hot rolling, cutting of pillars for dilatometry, solution treatment at 1250 °C, hot compressive deformation in the dilatometer, isothermal holding for 100 s at 900 °C, and quenching to room temperature.

Specimens for study in the TEM were prepared using the Focused Ion Beam (FIB) lift-out technique in an FEI Nova 200 Nanolab Dualbeam FIB. The procedure was optimised using methods adapted from Schaffer et al. [13] using low voltages in the latter stages to avoid significant Ga implementation and other FIB artefacts such as surface defects. The surface was additionally protected by the evaporation of about 30 nm of gold, prior to platinum deposition in the FIB, to reduce both Pt redeposition onto the sample and curtaining because of the granular structure of the electron beam deposited platinum.

2.2. Instrumentation and experiment

Initial investigations were carried out using an FEI Tecnai T20 equipped with a Gatan GIF2000 energy filter. Dark field imaging and diffraction analysis showed that the precipitates had a cube-on-cube orientation relationship with the matrix. These investigations also showed that there was often a thin, surface layer of Fe_3O_4 with a well-defined orientation relationship to the underlying matrix. Energy filtered images of the TEM samples were used to identify areas of the specimen which contained suitable precipitates. This was particularly helpful for the V steel since there is very little contrast between VC and the matrix in the high angle annular dark field (HAADF) imaging mode of STEM, which makes locating precipitates very difficult in STEM mode.

EELS-SI investigations were performed on a probe-corrected JEOL ARM 200F equipped with a cold field emission gun (CFEG) and operated at 200 kV. It was fitted with a Gatan GIF Quantum ER energy filter/spectrometer equipped with a fast DualEELS system allowing the rapid acquisition of spectrum image data containing both the low loss and core loss regions of the spectrum at each pixel [8]. The STEM data were recorded using a suitable condenser aperture to give a convergence semi-angle of 29 mrad, which includes the mostly flat area of the centre of the Ronchigram and excludes the highly aberrated portion of the Ronchigram at higher angles—these conditions should allow a probe size of down to 1–2 Å, even at higher probe currents. A probe current of approximately 400 pA and a spectrometer acceptance semi-angle of 36 mrad were normally used. The dispersion was set at 0.5 eV/channel and spectra with 2048 channels were recorded so that the energy range in each spectrum was 1024 eV. All acquisitions were performed using the spectrum imaging plug-in for Gatan

DigitalMicrograph (DM). The zero loss peak (ZLP) was positioned in the low loss spectrum so that there were sufficient channels on its low energy side to allow the correction of the bleed-through artefact, where required. The start energy of the core loss spectrum was offset by applying a known voltage to the drift tube of the spectrometer. This voltage was chosen to give enough channels prior to the first edge of interest (the C K-edge for the V steel and the Nb M_{4,5}- edge for the Nb steel) to allow splicing and background fitting without disturbing this edge. The integration times were set so that the counts in the most intense channel (the zero-loss peak (ZLP) in the low loss region and the low energy end of the core loss region were just below the saturation level of the CCD. This required times of tens of microseconds for the low-loss spectra and tens of milliseconds for the core-loss spectra. Total acquisition times for a map of 50–100 pixels square were of the order of a few minutes. The typical spacing of pixels in a spectrum image was of the order of 0.3–0.5 nm. Where possible, drift correction was not used, since this allows quicker acquisition and stage stability was often good enough to allow this. Where absolutely necessary, drift correction was carried out at the beginning of each line. At the end of each acquisition, the dark current correction was optimised using the high quality dark reference correction function in Gatan Microscopy Suite (GMS) 2.3. This averages many dark references to give a final dark reference that has significantly reduced noise. Specific experimental conditions are given below.

Minimisation of carbon contamination was essential to performing good quality spectrum imaging. The sample and holder were cleaned in an oxygen/argon plasma prior to insertion into the microscope. Additionally, prior to recording data from any sample, the whole sample was irradiated by electrons (flooding) to polymerise any mobile hydrocarbon in the form of a very thin layer all over the specimen.

3. Post-processing procedure

Post-processing of the resulting datasets is performed in GMS 2.3 using a combination of inbuilt routines and custom scripts. The procedures are described in the five sub-sections below. Depending on the specific dataset, the order of individual procedures may be changed if it improves the outcome. The first sub-section describes the steps necessary to reduce the noise using PCA. The second describes how to obtain good spliced spectra at each pixel and apply Fourier log deconvolution. The third describes how to remove the matrix contribution. The fourth describes how to fit backgrounds to the edges of interest in the V steel to give the edge intensities how to correct these intensities for the contributions from the residual oxide and amorphous carbon. The fifth describes the equivalent procedures for the Nb steel.

Whilst the work performed here was performed using both standard functions and custom scripts for GMS 2.3, it would of course be possible to perform exactly the same operations using any package for the processing of spectrum image data, such as Hyperspy [14]. Exact technical details for GMS 2.3 are given since most readers who have access to the hardware required to do this kind of work will also have access to this software, and this will therefore aid many readers in adapting these methods to their own scientific challenges.

3.1. Noise reduction by PCA

The outcome of PCA noise reduction is found to be more successful if the x-ray spikes caused by spurious external radiation and the energy shifts caused by instrumental instabilities are first removed. In the case of the x-ray spikes, we used the inbuilt

routine in GMS 2.3 “Volume → Remove X-rays”, the routine looks for sharp localized features in the spatial plane at each energy loss and replaces them with values representative of the intensities on either side. In terms of removal of the effects of instrumental instabilities, the ZLP acts as a self-calibration for the low loss region and so the low loss spectra are shifted so that the ZLP occurs in the same spectrum channel at each spatial pixel using the GMS function “SI → Align SI by Peak”. Since the core loss spectrum is recorded within a short time of the low loss spectrum in DualEELS, it is assumed that the shift required for the core loss spectrum is the same as that required for the low loss at the same pixel. After this re-alignment, the peak of the ZLP is calibrated to be zero and, in the ideal case, the equivalent channel in the core loss spectrum is calibrated to a value equal to the offset voltage applied to the spectrometer drift tube. However, because of the non-linear dispersion in the spectrometer, this results in all edges being slightly miscalibrated in position. Thus, as a standard measure, the onset of the Fe L₃ white line was set to 708 eV. Below this energy, this results in edges appearing at energies slightly different to their tabulated values.

The realignment of the spectra causes a small range of channels at each end of the spectra to contain unreliable data. In addition, two other effects can be dealt with at this point: one is the loss of detection efficiency at the ends of the spectrum due to shadowing, and the other is there can be areas of the spectrum image where the acquisition was corrupt for one reason or another. If not removed, these effects can cause problems in subsequent processing. The “Volume → Extract → Extract Volume” function in GMS 2.3 is used to select the central region of the dataset where these effects are not present and thereby cut of the outside edges containing the alignment and other artefacts.

PCA is then applied separately to both low loss and high loss datasets. This separates the real spectroscopic signals from random noise in the datasets [11] using the Multivariate Statistical Analysis plug-in of Lucas et al. [15] for GMS 2.3.

While this approach works well for the V steel data, PCA does not significantly reduce the noise in the low loss data from the Nb steel. Here, a big improvement in noise reduction by PCA is found if the region prior to the zero loss peak and that above 250 eV (well above the splice point energy) are removed from the data prior to using PCA. Fig. 2 shows that these regions contain no important information but very significant noise – this noise can appear as many significant components in the PCA decomposition, unless these regions are removed prior to running PCA. However, in order to do this, the correction for the core loss bleed-through described in the next section must be applied first, if required.

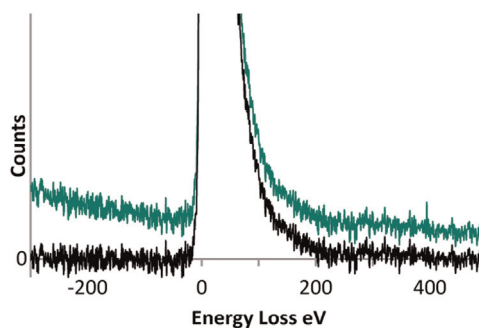


Fig. 2. The effect on the low loss spectrum of the bleed-through between the core-loss and low-loss regions (green, grey in print), together with the corrected low-loss spectrum (black).

3.2. Splicing the low and core loss regions and Fourier logarithmic deconvolution

In Fig. 2, the spectrum in green shows the effect of the bleed-through of the core loss region into the low region. This is significant in many but not all datasets. It is believed to arise as a result of multiple backscattering in the spectrometer detector chamber and is not simply from misalignment of the beam trap – this has since been improved in the Glasgow spectrometer by some alterations to the camera chamber. Significant bleed-through has two significant effects on subsequent processing. The first is that it gives a major error in the determination of t/λ from the low loss spectrum, since the DM2.3 function for this assumes that the spectrum has a true zero value. The second is that it perturbs the slope of the low loss spectrum in the region of the splice point. It is unclear how widespread such problems are with DualEELS spectrometers, but as shown below it is possible to subtract such signals from the datasets to allow quantitative processing.

An empirical correction procedure is adopted which uses the power law background fitting routine in DM2.3. To reduce the effect of noise in the correction, the low loss spectra from all the spatial pixels in the spectrum image are summed. The left hand edge of this sum spectrum is then temporarily calibrated to be at an energy that results in a good fit of the power law function in the region in front of the ZLP. This background is assumed to represent the average shape of the bleed-through contribution and is divided by the number of spatial pixels to give an average contribution at each pixel. At this point, there is a choice between either simply subtracting this average contribution from the low loss spectrum at each spatial pixel or scaling it to match the intensity prior to the ZLP in each spectrum prior to subtraction. The former choice works well for our datasets, which are just a few tens of nm in size. This approach avoids the uncertainty scaling to individual spectra in regions where the signal has significant noise. However, for larger map areas with noticeable elastic contrast, this might be too crude and so the scale and subtract approach might be needed. A typical corrected spectrum is shown in black in Fig. 2.

Fig. 3 shows the result of splicing the core loss region and the low loss region after correction for the bleed-through. The noise in the low loss region in the vicinity of the splice point gives considerable uncertainty in the scaling factor and leads to steps in the spectrum whose size varies from spatial pixel to spatial pixel depending on the precise details of the splicing procedure. The thin black line in the high loss region shows this in an exaggerated fashion by splicing at a minimum in the noise. However, in most cases, and certainly for the two steels here, there is a region prior to the splice point that contains no information. Thus the effect of the noise can be minimised by fitting a power law in this region

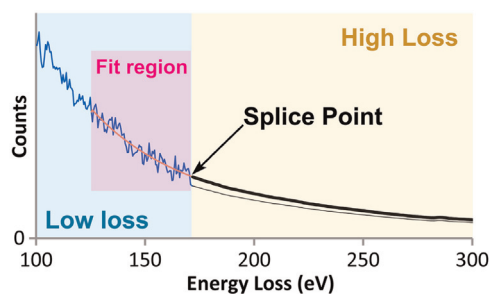


Fig. 3. Comparison of splicing the low loss and core loss regions of the spectra without and with prior smoothing of the end of the low loss spectrum using a power law fit. Details can be found in the text. The raw low loss data is shown in blue (dark grey in print), the smoothed low-loss in red (light grey in print), the spliced high-loss to the raw low loss in thin black, and the spliced high loss to the smoothed low-loss in thick black.

and replacing the actual low loss data by this fit as shown by the red line in Fig. 3. The low loss and core loss regions can then be spliced at a single point and will fit without any discontinuity, as shown by the thick black line in Fig. 3. The result is called the spliced spectrum image. This approach to naming datasets is used below to indicate the point in the processing associated with a particular spectrum image.

The next step is to remove the effects of plural scattering using the Fourier logarithmic deconvolution [12]. This provides several important advantages for later process steps. The low loss shape can change due to variations in the specimen thickness (including the effect of carbon contamination) or changes of composition (e.g. the presence of the precipitate in the matrix). This changes both the shape of the edges and the shape of the background in the spectra. Thus, removing the plural scattering helps in scaling and subtracting the matrix contribution since the shape of the edge from the matrix is now the same at all pixels. It also allows the use of standards taken under different conditions provided they have also had the plural scattering removed. Finally, it improves power law background fitting particularly if the sample is not ultra-thin.

For straightforward mathematical reasons, the Fourier logarithmic deconvolution function in DM gives artifacts if there are negative counts in the data. Fig. 2 shows that negative counts are present on the left hand side of the ZLP after correction for the bleed-through. Thus, prior to the deconvolution, the “Volume → Extract → Extract Volume” function of GMS 2.3 is used to extract just the region of the spectrum image that does not contain negative counts.

Associated with the deconvolved spectrum image is a spatial map of the integrated ZLP intensity at each pixel. This is used in the quantification of processed spectrum images both to calculate the thickness of the precipitate at each spatial pixel from the low loss (used both later in this paper and in part 2) and the absolute numbers of atoms in the precipitate at each pixel from quantification of core loss edges (used in part 2 of this publication).

3.3. Estimation and removal of the matrix contributions

Fe is the major element in the matrix and is either absent from the precipitates or present in very low concentration [4]. Thus the approach to removing the matrix contribution is to create an average spectrum representative of the matrix composition in the deconvolved spectrum image. To allow subsequent scaling, this is normalized by its background subtracted Fe $L_{2,3}$ intensity integrated over a given window. Typically a 50 eV wide integration window starting at the $L_{2,3}$ threshold is used. A dataset, the matrix spectrum image, is generated with the same spatial array of pixels as the deconvolved spectrum image but with the normalized matrix spectrum at each pixel.

Using the deconvolved spectrum image, a map of the background subtracted Fe $L_{2,3}$ intensity is made using the same background and signal integration windows used to generate the normalised matrix spectrum image. The intensity in a pixel of this map is then used to scale the spectrum in the equivalent pixel in the normalised matrix spectrum image so that its Fe $L_{2,3}$ intensity matches that in the equivalent pixel of the deconvolved spectrum image.

This scaled matrix spectrum image is then subtracted from the deconvolved spectrum image to leave the precipitate spectrum image. In the ideal case (Fig. 1a, c), this would only contain information about the precipitate. However, the presence of surface oxide and amorphous carbon means that it contains contributions from these other sources too (Fig. 1b, d).

In practice, the varying thickness of the amorphous carbon can create difficulties in the process described above. If the region from which the average matrix spectrum is extracted has a varying

thickness of amorphous carbon, then the intensity of the C K-edge in some pixels will be greater than in the corresponding pixels of the deconvolved SI. After subtraction, this will leave the spectra in some pixels of the precipitate spectrum image with regions of negative intensity and this may cause issues with subsequent processing.

To minimise such issues, an average matrix spectrum is made from only pixels with a low carbon signal. To do this, a map of the background subtracted C K-edge-intensity is made from the deconvolved SI. A binary mask is then generated from this map. The mask is 1 where the C K-edge intensity is less than a chosen intensity level and 0 elsewhere. The threshold for creating the mask is set to give 1 at enough pixels to give a good average spectrum, whose noise will be less than that in the spectrum from a single pixel. The spectra in the deconvolved spectrum image are multiplied spatial pixel by spatial pixel by the values in the mask, leaving only those spectra with a low C K-edge intensity. After applying the mask, the remaining spectra are summed and normalized as described above and the rest of the procedure performed. In the resultant precipitate spectrum image, there are regions where the contribution to the precipitate spectrum image from amorphous carbon are essentially zero and others where there are significant contributions from amorphous carbon but there are only a small number of pixels with spectra with negative counts.

The main part of Fig. 4 shows the summed spectra from 5×6 pixels in the centre of a V(C,N) precipitate in the precipitate SI. The spectrum shown in red (grey in the print version) is that after splicing and deconvolution. The C K-edge, the Ti $L_{2,3}$ -edges, the V $L_{2,3}$ -edges, the O K-edge, the Mn $L_{2,3}$ -edges and the Fe $L_{2,3}$ -edges can be clearly seen. The black spectrum is from the same region after subtraction of the matrix contribution. At the positions of the Fe and Mn $L_{2,3}$ -edges, there is only a small perturbation due to errors in the subtraction in the neighbourhood of the sharp white lines. The intensity of the O K-edge immediately after the V $L_{2,3}$ white lines has diminished significantly. The ELNES on the C K-edge is much clearer and the background under all the remaining edges is much reduced.

The inset shows the comparison of the low-loss region in the deconvolved and precipitate spectrum images. It may be noted that the intensity has dropped dramatically, showing that the most of the sample thickness was matrix. Also, the bulk plasmon has shifted slightly, and the Mn and Fe- $M_{2,3}$ edges at just above 50 eV have disappeared leaving the Ti and V $M_{2,3}$ -edges much more visible.

The relative thickness map of the precipitate in units of t/λ [12] can be obtained at each spatial pixel by integrating the intensity of the spectrum at that pixel in the precipitate spectrum image and

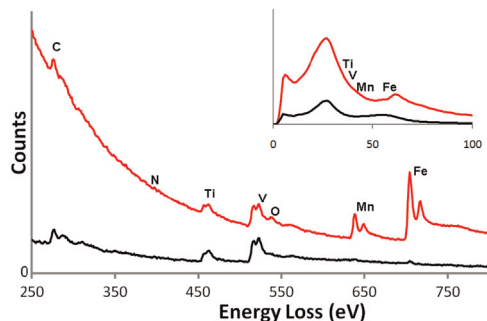


Fig. 4. The effects of matrix subtraction on the summed spectrum from 5×6 pixels in the centre of a (V,Ti)C precipitate. The deconvolved spectrum without removal of the signal from steel matrix is shown in red (dark grey if printed in black and white). The spectrum after removal of the matrix contribution, i.e. the (V,Ti) precipitate only, is shown in black. The low loss region is shown in the inset.

dividing it by the value in the equivalent pixel of the map of the integrated ZLP intensities associated with the deconvolved spectrum image.

3.4. Background fitting and edge intensities in the V steel

The standard procedure for removing the background under an EELS edge is to fit a power law background to a region before the edge and extrapolate the fit function under the edge [12]. For this to be successful, the background shape in the fitting region must have this power law dependence (i.e. $I = A E^{-r}$). The wider the energy over which a good fit can be made, the more reliable the estimated background (especially in the presence of noise). A good background fit should leave noise which varies randomly about zero in the fitting region but shows no overall shape in the residuals. Varying the width and position of the window slightly should make a minimal difference to the fit.

A number of factors can prevent such a good fit being obtained. If there is a lower lying edge close to the edge of interest, the overall shape of this edge, its ELNES or its extended energy loss fine structure (EXELFS) can perturb the background shape in front of the edge of interest. If the specimen is relatively thick, plural scattering can also modify the background shape. This is more of a problem for moderate energy losses (up to a few hundred eV), where the background slope changes on the scale of the plasmon energy, whereas, at higher losses, the background slope changes more slowly and is little affected by plural scattering.

Fig. 5 shows examples of background subtracted spectra from a few pixels in the centre of the precipitate. This precipitate had a t/λ of 0.07 in a specimen with an overall t/λ of ~ 0.4 . Each edge is shown at three stage of the processing: after splicing (light green, light grey in print); deconvolved (red, dark grey in print); and after removal of the matrix contribution (black). Fig. 5a is the C K-edge, Fig. 5b the N K-edge, Fig. 5c the Ti $L_{2,3}$ -edge, Fig. 5d the V $L_{2,3}$ -edge, Fig. 5e the V L_{1} -edge and the Mn $L_{2,3}$ -edge, and Fig. 5f the Fe $L_{2,3}$ -edge. The background fitting window is shown in pink (light grey). The signal integration window used for the maps in Fig. 9 is shown above the edges in green (very pale grey in print).

Fig. 5e and f shows that the Fe and Mn signals are very effectively removed by the matrix subtraction, as expected. The Mn $L_{2,3}$ -edge sits on top of the V L_{1} -edge at 628 eV and the signal from the latter edge remains after the matrix subtraction.

In samples with a t/λ approaching 1, deconvolution often improves background fitting before EELS edges. However, in this sample, there is little apparent improvement in the quality of the background fit after deconvolution as the total amount of multiple scattering is low. Nevertheless, deconvolution does have a more subtle effect. Comparing the fractional changes in edge intensity before and after deconvolution, that for the Ti edge is small, that for the V edge is large and those for the Mn and Fe edges are medium and similar. The fractional change in the edge intensity caused by the deconvolution would be expected to be very similar if caused solely by multiple scattering of the edge signal. The explanation for the differences is that the deconvolution process also modifies the background shape in front of the edge. The Fe and Mn edges are well separated and at higher energies and so the changes in background shape would have least effect. However, since the V edge sits on the tail of the Ti edge, the background shape before the V edge will be the most changed leading to the largest fractional change in the edge intensity. On the other hand, the fractional change in the Ti edge is small because the background in front of the edge is made less steep by the multiple scattering. Thus, in the un-deconvoluted spliced data, the signal extracted from Ti edge is reduced as the energy loss increases, leading to the smaller difference between this edge and that extracted from the deconvoluted data.

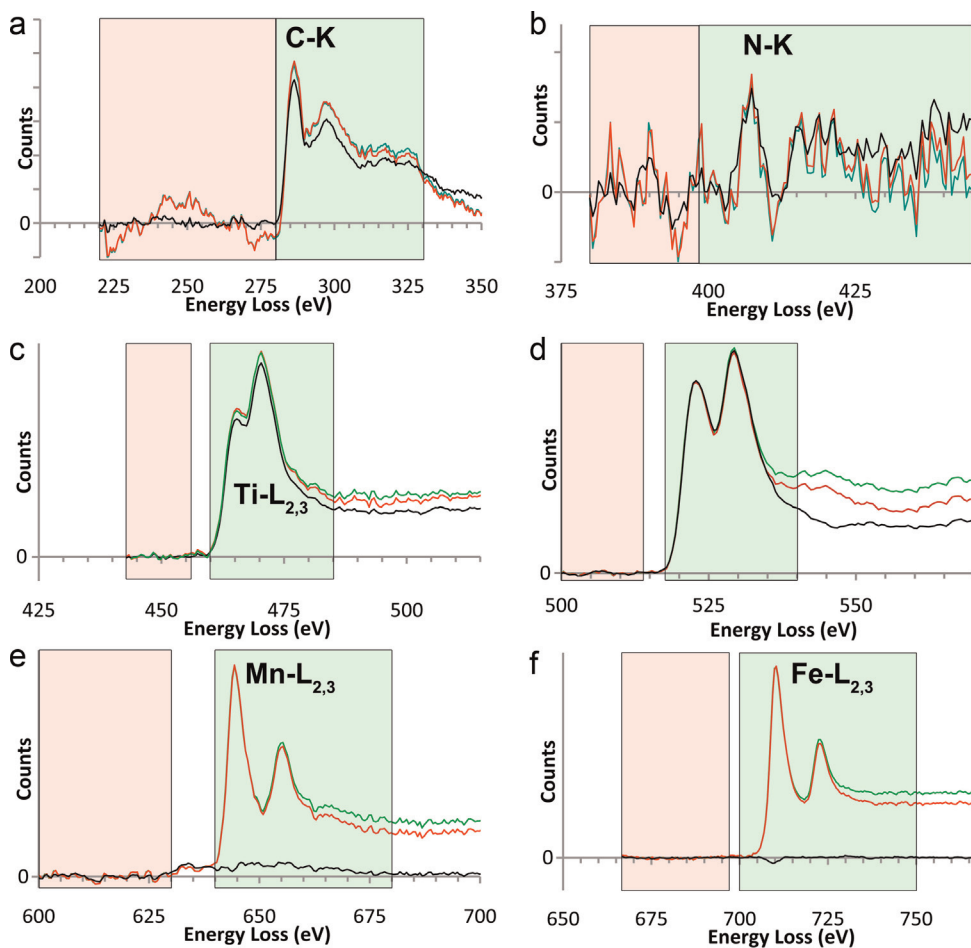


Fig. 5. Edges intensities extracted at three points in the processing: after splicing (green / light grey in print); after deconvolution (red / dark grey in print); and after removal of the matrix contribution (black). a) the C K-edge; b) the N K-edge; c) the Ti $L_{2,3}$ -edge; d) V $L_{2,3}$ -edge; e) the V L_{1} -edge and the Mn $L_{2,3}$ -edge; f) the Fe $L_{2,3}$ -edge. The background-fitting window is shown as a pink box on each plot (pale grey in print). The signal integration windows used for the maps in Fig. 9 are shown as boxes above the edges in pale green (very pale grey in print).

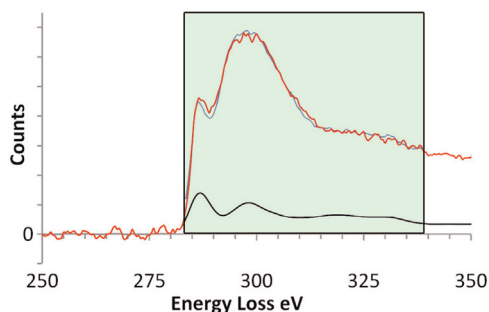


Fig. 6. The background subtracted C K-edge shape from the precipitate spectrum image is shown in red (dark grey in print). It is the sum of spectra over several pixels in the centre of the precipitate. The MLLS fit to this edge is shown in blue (light grey in print) and the fitting window in pale green (pale grey in print). The contribution of the shape of the C K-edge shape from VC is shown in black, and this is the signal of interest. The difference between this and the MLLS fit is the contribution from surface amorphous carbon. (Note, this result is taken from a dataset where there was significant carbon build-up in order to illustrate the point).

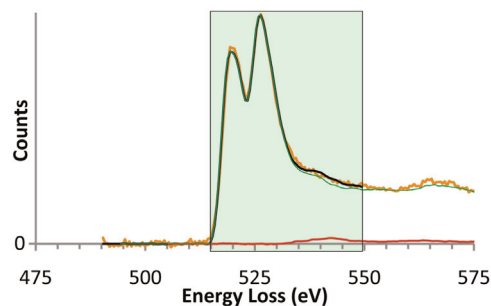


Fig. 7. MLLS fitting to separate O from the V signal for a VC precipitate. The raw signal is shown in gold (light thick grey in print), the MLLS fit in black, the O component of the fit in red (dark grey in print), and the V component in green (light grey in print) (the MLLS fit window is in pale green (pale grey in print)). The O-K standard was selected from within the spectrum image from an area containing no precipitate, and the V- $L_{2,3}$ standard was from previous work on bulk VC [17].

The situation for the C and N edges is more complicated. Fig. 5a shows the background shape before the C-K edge is still far from the ideal power law shape after deconvolution. The perturbation to the background shape is caused by strong extended energy loss fine structure (EXELFS) from the Mn and Fe M edges causing oscillations in intensity about the power law shape. Subtraction of

the matrix contributions removes these oscillations and the background before the C-K edge now behaves according to a monotonic power law, giving a good background fit. The C K-edge no longer goes negative after background subtraction, giving a much more reliable extraction of the C-K edge for detailed analysis or quantification.

This subtraction of the matrix contribution also has major benefits around the weak N edge. Prior to subtraction of the matrix contribution, the intensity of the extracted N edge becomes

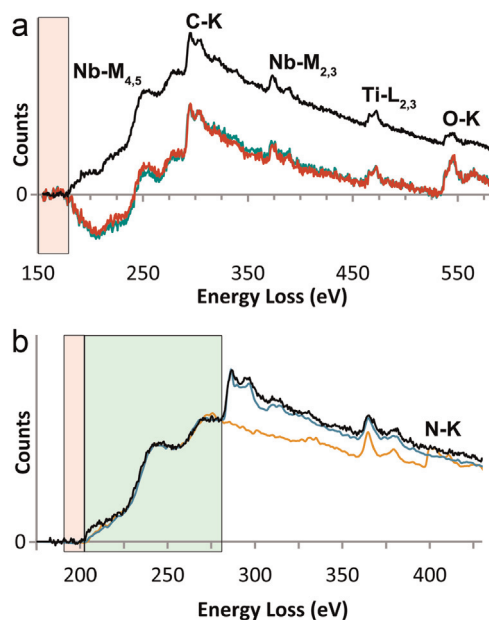


Fig. 8. (a) The results of background subtraction using the fitting window indicated by the pale pink box (pale grey in print) in front of the Nb- $M_{4,5}$ edge on a sample with a total t/λ of 0.18. Each is shown at three stages of the processing: after splicing (green, light grey in print); after deconvolution (red, dark grey in print); and after removal of the matrix contribution (black). (b) The result of background subtraction using a smaller fitting window closer to the Nb $M_{4,5}$ -edge, again indicated by the pale pink box (pale grey in print). A comparison is made of the edge shapes from the precipitate (black) with those from NbC (dark aqua/dark grey) and NbN (gold / light grey in print) standards with similar background fitting windows and scaled to have the same integrated Nb- $M_{4,5}$ intensity prior to the C-K edge. The signal integration window for the Nb maps in Fig. 10 is shown by the pale green box (very pale grey in print).

negative before the Ti edge. After removal of the matrix contribution, it remains positive right up to the Ti edge and allows the improved mapping of the N edge intensity demonstrated below. Integrating the C and N signals over 50 eV windows and using Hartree-Slater partial cross-sections, gives the N:C ratio as approximately 1:6. Using the Iakoubovskii et al. [10] parameterisation of the experimental mean free path data, the thickness of the precipitate is ~ 8 nm and the overlying matrix is ~ 37 nm. Assuming that the materials are viewed along their [100] crystal directions, there would be ~ 106 metal sites along an atomic column in the matrix and ~ 20 anion sites in the precipitate. Of the latter, ~ 3 are N amounting to ~ 2 at% of the sample, and this gives an estimate of the sensitivity achieved.

The V $L_{2,3}$ edge also benefits significantly from the subtraction of matrix contributions, since some of the signal from the O present as surface oxide is subtracted when the matrix contribution is removed. Fig. 5d shows a very significant decrease in the O K-edge intensity after the V L_3 and L_2 white lines.

It is clear that removal of the matrix signal gives improved signal extraction for the elements in the precipitate. However, it still leaves residual contributions from the surface oxygen and carbon. The procedure for correcting for these contributions is now considered.

If there is carbon contamination, the intensity in the C K-edge will be a mixture of contributions from the carbon in the precipitate and that in the amorphous carbon. These have very different ELNES and this can be used to estimate the two contributions [16]. A more quantitative approach is to use multiple linear least squares (MLLS) fitting of edge shapes from standards. The edge shape from amorphous carbon can be extracted from the matrix region of the deconvolved spectrum image. Ideally the edge

shape for the carbon in the precipitate should be taken from spectra recorded from an isolated precipitate of the same composition, using the same experimental conditions and processed in the same way.

Unfortunately, such a standard is not available. However, data for VC are available. These were recorded previously in a VG HB5 STEM with post-specimen lenses and a Gatan 666 PEELS spectrometer operated at 100 keV. A probe half-angle of 11 mrad and a collection half-angle of 12.5 mrad were used. The data processing used is described in Craven and Garvie [17] and the plural scattering has been deconvolved. Provided that the data are recorded over a range of scattering angles large compared to the characteristic angle, ϑ_E , the edge shape is relatively insensitive to the experimental conditions. $\vartheta_E = \Delta E/2E$ where ΔE is the energy loss of the edge and E is the energy of the electron probe. For the C K-edge this has a value of 0.7 mrad at 200 keV and 1.4 mrad at 100 keV. These values are much smaller than the experimental angles used in the respective acquisitions. Hence the VC data from the HB5 should act as a reasonable standard for VC recorded in this work. A complicating factor is that the precipitate contains both Ti and N. However, there is much more V than Ti and very much more C than N. Since the shapes of the C K-edges in VC and TiC and the shapes of the C and N K-edges in VC and VN are relatively similar [17,18], the carbon edge shape from VC should provide a reasonable standard for the C K-edge in the precipitate.

As there is only a very small contribution from amorphous carbon in the data shown in Fig. 5, a dataset in which there had been significant build-up of amorphous carbon is used to illustrate the procedure. The red line (dark grey) in Fig. 6 shows the background subtracted C K-edge summed over 5 by 6 pixels from the centre of the precipitate. The blue line (light grey in print) shows the MLLS fit to the data using the two standards described above. The fit was carried out over the energy range shown by the pale green rectangle (pale grey). Note the close agreement of the fit and the standard. The contribution to the MLLS fit of the VC standard is shown in black. This is the best estimate of the C K-edge intensity from the precipitate alone. With this level of amorphous carbon build up, there will be a significant uncertainty in the intensity of the carbon K-edge from the precipitate and so every effort should be made to limit the carbon contamination when collecting the data.

In a similar way, the residual O K-edge can be separated from the V $L_{2,3}$ -edges using MLLS fitting of the spectra in the spectrum image as a weighted sum of the O K-edge shape from the matrix-only regions of the spectrum image and the V $L_{2,3}$ -edge shape from the VC standard above [17]. The results are shown in Fig. 7 for the V edge in Fig. 5. The residual O signal is small since the majority of it was removed by the earlier subtraction of the matrix signal.

3.5. Background fitting and edge intensities in the Nb steel

In the Nb steel, the issues are slightly different. Extraction of the C K-edge intensity is complicated by the fact that the C K-edge sits on the Nb $M_{4,5}$ -edges, which makes the background subtraction much more difficult. The problem of the effect of carbon contamination remains but the level of carbon contamination is much lower in the best datasets from this steel. This is because the datasets were recorded later in the study, at which point the contamination-control was much better. As there is no V in the steel, it is not necessary to correct for residual O. So far, no N K-edge has been reliably detected in this steel.

Fig. 8a shows the results of background subtraction using the window shown in by the pale pink box (pale grey) in front of the Nb $M_{4,5}$ -edges. The sample has a total t/λ of 0.18 and the precipitate has t/λ of 0.08. Again, the results are shown at three stages of the processing: after splicing (green/light grey); after deconvolution

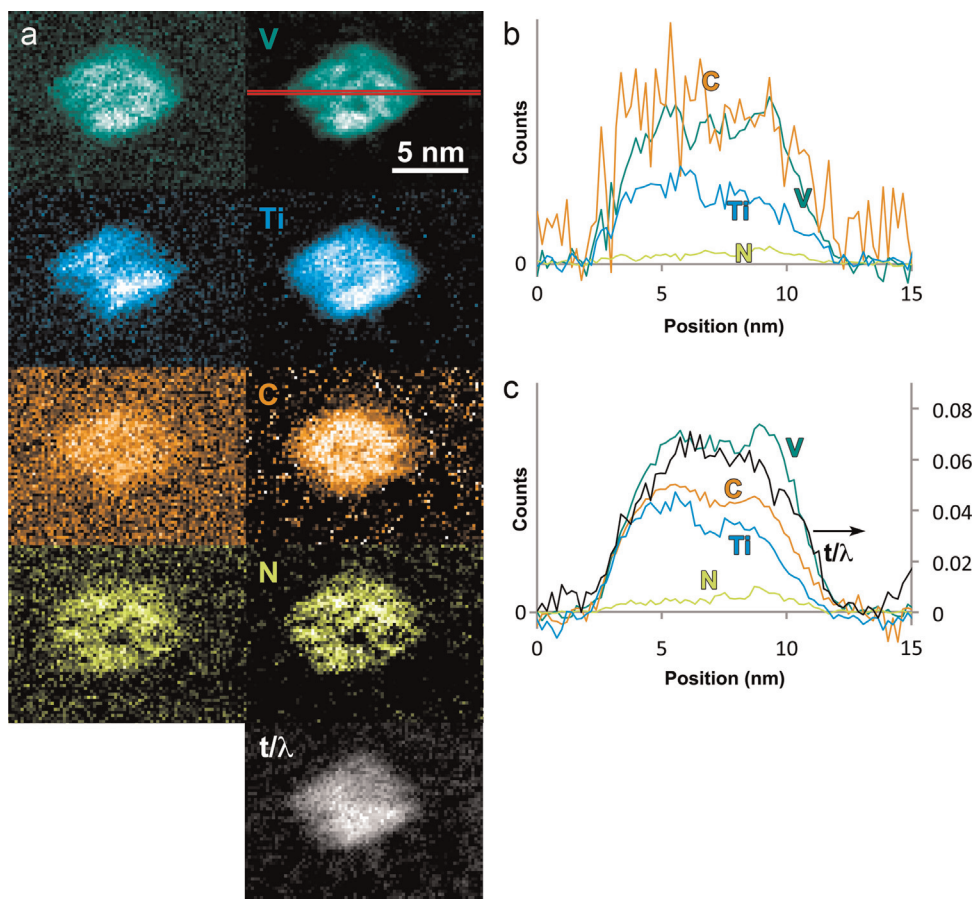


Fig. 9. a) Maps of the edge intensities for a precipitate in the V steel: left column from the as-recorded data with no corrections; right column from the fully processed data (both using the same background fitting and signal integration windows). Black in the maps corresponds to zero counts. b) Line profiles across the maps from the unprocessed data (colours as for the maps in a), the position of the line for the profile is shown in the upper right V map. c) Line profiles across the maps from the fully processed data; the elemental signals are plotted against the left hand y axis and the thickness plot (black) is plotted against the right hand y axis.

(red/dark grey); and after removal of the matrix contribution (black). Both before and after deconvolution, the background fit is very poor resulting in significant negative intensity at the start of the edge. It is impossible to find a background estimation window that gives a well-behaved background subtraction for such data. As with the V steel, the major issue here is the EXELFS from the Mn and Fe $M_{2,3}$ -edges. Subtraction of the matrix contribution is hugely beneficial as it removes the EXELFS from the Mn and Fe that perturb the background before the Nb- $M_{4,5}$ edge [19]. The black spectrum in Fig. 8a shows a good background fit after the subtraction of the matrix signal.

However, the upper edge of the background window used is at ~ 180 eV and the Nb $M_{4,5}$ -edge onset is ~ 205 eV. The intensity before the edge threshold cannot be attributed to an edge from another element in the system. It is likely that it is a contribution from the EXELFS of lower-lying Nb N-edges. The black spectrum in Fig. 5b uses a narrow background window immediately before the $M_{4,5}$ edge. Also shown on Fig. 5b are spectra from NbC (red/dark grey) and NbN (green/light grey). These spectra were recorded in the HB5 using the same experimental conditions given above for the VC data [17,18]. A narrow background fitting window in front of the Nb $M_{4,5}$ -edges was also used for these edges and they are scaled to have the same Nb $M_{4,5}$ -edge intensity prior to the C K-edge. There is good agreement between the spectrum from the precipitate and that from the NbC standard but the intensity of the C K-edge is systematically slightly higher in the precipitate. This additional intensity is likely to be because the precipitate contains a small fraction of Ti, which will increase the C:Nb ratio over that for pure NbC. Subtracting the background under the C K-edges

using a power law background is challenging in this case. However, the scaled NbN spectrum in Fig. 5b provides the shape of the Nb $M_{4,5}$ -edges under the C K-edge and can be subtracted to give the C K-edge intensity.

4. Precipitate maps and profiles

4.1. Precipitates in vanadium steels

The effect of the digital extraction replica technique on the resulting maps in a vanadium steel is shown in Fig. 9. The dataset is the same as that used for to give the edge shapes in Fig. 5, where the signal integration windows are shown. In all the maps, black corresponds to a signal of zero. The left hand column shows V, Ti, C and N maps calculated from the original raw EELS-SI dataset using a standard power-law background fit and the same background and signal windows as for the digitally extracted dataset. The right hand column shows the same maps extracted from the digitally extracted precipitate spectrum image plus the t/λ map for the precipitate. This final map can only be obtained with such processing.

The V map is already clear in the raw data but is exceptionally clear and with low noise after the extraction processing. The Ti, which is present at a lower level, gives a noisier map in the raw spectrum image but is much clearer with similarly low noise to the V map when the fully processed data are used. Extracting the C signal from the as recorded data is problematical. The poor background subtraction, combined with any surface carbon present,

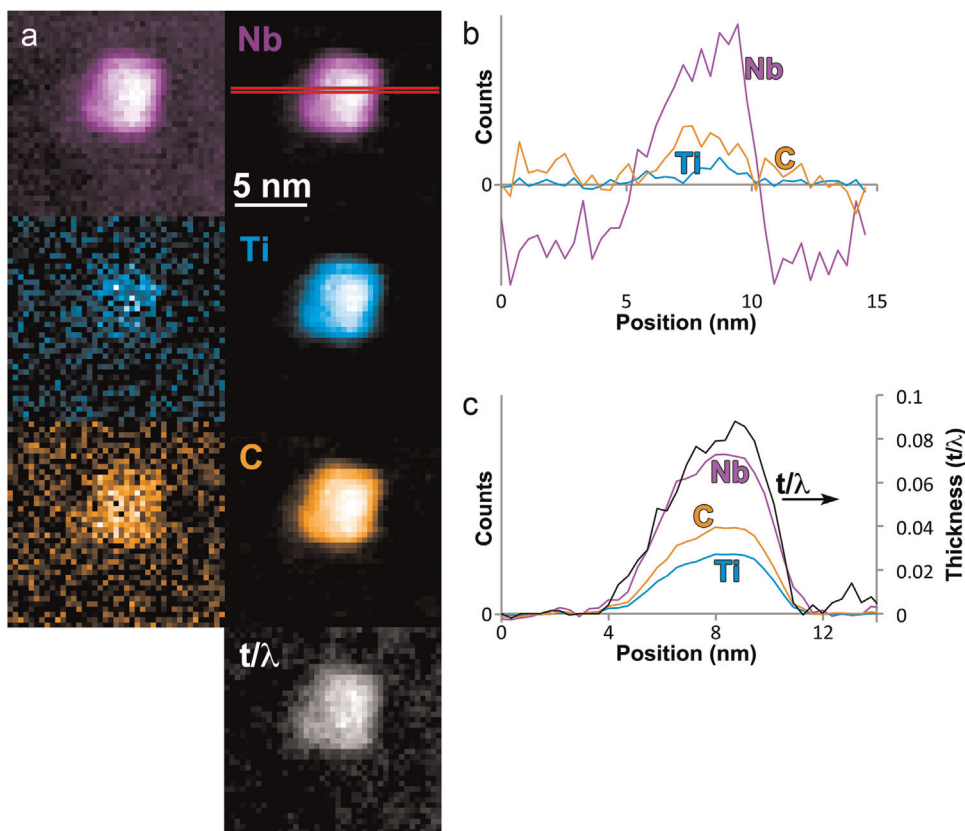


Fig. 10. a) Maps of the edge intensities for a precipitate in the Nb steel: left column from the as-recorded data; right column from the fully processed data. Black in all maps except the Nb map from the raw data corresponds to zero signal; the raw map of Nb has a large offset from zero due to a poor background fit so the black level is set at the average Nb signal level outside the precipitate (otherwise the edges of the precipitate would be lost in the map). b) Line profiles across the maps from the unprocessed data (the position of the line for the profiles is shown in the upper right Nb map). c) Line profiles across the maps from the fully processed data.

appear to give a C signal everywhere. A much clearer C map, with similarly low noise to the V and Ti maps, results from the fully processed precipitate spectrum image. A N signal can be mapped in the raw dataset, although it is only just emerging from the noise. After digital extraction, it is possible to map N much better, and with much reduced background noise due to the more reliable background fitting. Considering that the N signal in each pixel of the map comes from a very few N atoms, the power of the processing procedure is clearly demonstrated.

The improvement in the quality of the maps is emphasised by the comparison of the profiles through the maps shown in the graphs in Fig. 9b and c. All the profiles are taken from the position of the line shown in the V map to the top right. Fig. 9b shows the much noisier profiles through the maps from the raw datasets and Fig. 9c shows the significant improvements achieved using the fully processed precipitate spectrum image. The profile of t/λ through the precipitate is also shown in Fig. 9c for comparison with the elemental signal profiles. It can be seen that this profile matches very well to the form of the elemental profiles.

It is clear from the maps that the elemental distributions are more or less homogeneous. While there may be local variations in the atomic ratios within the precipitate, there is no evidence of a classical core-shell structure in which a precipitate of one composition forms first and is then overgrown by material of a different composition [20].

4.2. Precipitates in Nb steels

The equivalent mapping for carbides in the Nb steel is summarised in Fig. 10 using the dataset from which the edges in Fig. 8 are taken. The integration window for the Nb $M_{4,5}$ -edges is shown

in Fig. 8. Similar integration windows to those shown in Fig. 5 are used to extract the signals from the other edges. Black in the maps corresponds to zero signal. As before, maps generated from the raw EELS-SI data are shown to the left and maps from the extracted precipitate spectrum image are shown to the right. The t/λ map is shown at the bottom of the right hand column. The Nb map from the unprocessed data is rather noisy and there are major problems with over-subtraction of the background outside the precipitate resulting in negative counts. This arises due to problems in the background fitting due to the EXELFS from lower lying edges as discussed above. In contrast to this, the Nb map after extraction of the precipitate spectrum image is much clearer, the precipitate is well defined and there is little problem with negative counts outside the precipitate. This suggests that the counts in the precipitate are being correctly determined and that the size and shape of the precipitate are now being accurately reproduced in the map. The Ti map from the raw data is almost unusable and there is just a faint hint of a precipitate there. This mainly occurs due to the noise in the raw data. This makes background subtraction before the Ti edge difficult and the varying background introduces a large amount of excess noise into the maps. After extraction of the precipitate spectrum image, the Ti extraction is straightforward and results in a high-quality, low-noise map with clear profiles, together with a baseline outside the precipitate which is very close to zero. The C map from the raw data is also very noisy and strongly affected by the problems of background subtraction due to the shape of the Nb $M_{4,5}$ edge. The corresponding map from the digitally extracted precipitate spectrum image is much clearer, with well-defined precipitate edges. The shapes of all the elemental profiles also match very well to the corresponding profile through the t/λ map.

In this precipitate, the elemental distributions are, if anything, more homogeneous than those in the precipitate in the V steel above. Thus, again, there is no evidence of a classical core-shell structure [20].

5. General discussion

It is shown that DualEELS datasets of suitable quality now allow the subtraction of matrix and other extraneous contributions to allow the extraction of a precipitate spectrum image, which is suitable for further quantitative evaluation. This builds on the earlier work of Craven et al. [3] in which it was shown that individual spectra from precipitates could be treated in a similar manner to allow subtraction of matrix contributions and the quantitative evaluation of precipitate chemistry. The advent of high-speed DualEELS, together with improvements in data processing routines (especially the use of Principal Component Analysis [11,15]) allow this to be carried out efficiently across whole maps. The benefits of this will include:

1. The ability to quantify the overall thickness profile of a buried feature such as a precipitate using the t/λ method [12]. This can be converted to an absolute thickness using an appropriate determination of λ . λ can be obtained using either an appropriate standard or using an appropriate parameterisation of experimental data. The recent parameterisation of λ in terms of experimental parameters and the sample density [10] seems to behave well in many cases, including at the higher probe and acceptance angles used in modern aberration-corrected STEM instruments.
2. The ability to quantify the total number of atoms in each pixel on an absolute scale, given an appropriate partial cross section for the edge of interest under the conditions used in the experiment and the window width used for integration. This is possible since the total incident intensity, I_0 , is known from the zero loss peak integral in the DualEELS dataset. However, since it is not clear what systematic errors will be present in any calculation of partial cross sections for specific edges, it will be necessary to calibrate these using appropriate standards. For example, the use of vanadium, niobium and titanium carbides or carbonitrides of known stoichiometry would be very useful in establishing the relevant cross sections for the precipitates studied in this work. The combination of an absolute quantification of atomic areal density with crystallographic parameters then allows the calculation of the precipitate thickness in terms of individual elemental contributions. For example, in our case, the addition of the quantified thickness for all metal cations in the rock-salt-structured carbide should allow the calculation of a total thickness, and this can be compared with the total thickness calculated from the t/λ method [12]. It would also be possible to calculate the total equivalent thickness for the carbon and nitrogen anions, although this may fall short of the total thickness, since such carbides are often known to be substoichiometric [21]. This will be discussed in more detail in part II, in which we will set out a standards-based absolute quantification methodology for such carbide precipitates in the digitally extracted precipitate-only spectrum images.

The method demonstrated here is widely applicable to other steels containing nanoscale precipitates, including HSLA steels, reactor pressure vessel steels, and oxide dispersion strengthened steels. It will work well in any case where the sample consists of a matrix or other dominating feature which contains a reasonable proportion of an element that is not present in the precipitate, inclusion or second phase. This would also apply in many cases of

heavy metal heterogeneous catalysts on supports, nanocomposites, and helium bubbles in irradiated materials. Thus, it is expected that this method will be of widespread applicability in many nanostructured, chemically inhomogeneous systems. However, it would be more difficult to apply where the same element is present in both the matrix and the precipitate or second phase, as is the case in many aluminium alloys.

Of course, there are further steps that can be taken to further improve the quality of the signal extraction. The “bleed-through” of background signal into the low loss spectrum in the acquisition of the DualEELS datasets needs to be minimised. Since this work was carried out, a redesign of an assembly in the spectrometer detector chamber by Gatan has now significantly reduced this bleed-through. As long as care is taken in spectrometer setup (specifically to ensure that the bright, low-loss region of the core-loss spectrum is fully absorbed in the beam trap), then it should be possible to acquire DualEELS datasets with minimal bleed-through.

Any non-linearity of the energy axis in the dataset causes problems with energy calibration and thus will affect the scaling factor at the splice point, as well as the number of counts in the channel relative to those in a channel of fixed width. These issues need to be addressed to obtain accurate quantification of the data. The alignment procedures for the GIF Quantum spectrometer have already been revised since the acquisition of the data presented here, and a realignment of the Glasgow spectrometer has already resulted in much reduced non-linearity across the spectrum (in some of the data recorded in this work at 0.5 eV per channel, the energy at about 200 eV energy loss could have been out by up to 8 eV, when the Fe L3 edge onset was set to 708 eV, but after realignment, all channels were within 1 eV of their correct value across the same range). Nevertheless, when working with very large energy ranges (e.g. at dispersions of 0.5 or 1 eV per channel), some non-linearity is inevitable (especially at the extreme ends of the ranges). Thus, it would be desirable in the future to develop a method for the measurement of the non-linearity and the subsequent re-binning and linearisation of the spectra as part of the data processing procedure. It should be noted that since realigning the spectrometer, the scaling factors at the splice point now match the timing ratios for the low loss and core loss datasets, thus showing that the mismatch was just caused by the non-linearity of dispersion in the original spectrometer setup.

Although procedures were included here to remove the effects of surface oxidation and carbon contamination, it would be better if there were no need to perform such corrections. Thus, improved sample preparation and handling to minimise surface damage, surface oxidation and contamination by volatile organics would help to ensure the best quality datasets and, consequently, the best quality extraction of the precipitate or inclusion signal from the matrix or support. This suggests that the use of optimised procedures for the use of low energy focussed ion beam milling [13] or the use of post-FIB low energy argon ion milling may be essential for achieving optimal sample quality to minimise sample damage and surface oxidation. Rigorous procedures for the minimisation of contamination such as sample storage protocols, plasma cleaning of the sample holder and sample, and vacuum baking of samples prior to microscopy, as well as the use of the “beam shower” in the microscope when necessary are essential for this kind of work. Finally, the acquisition of standard spectra from particles, precipitates or inclusions free of matrix contributions may provide useful standards for MLLS fitting when separating the particle spectrum image from other contributions to the total deconvolved SI and its subsequent quantification.

Finally, the thickness of the specimen should be chosen carefully. If it is too thin, the chance of finding precipitates within the field of view of the spectrum image is lowered (and the

contribution from any damaged surfaces of the specimen may be undesirably high). If it is too thick, it is more difficult to extract the data from each precipitate. Key factors in determining the optimum thickness will be the precipitate size and number per unit volume together with their spatial distribution in the material under study.

6. Conclusions

It has been shown that suitably acquired DualEELS spectrum images around buried nanoscale precipitates in a matrix can be processed in such a way that allows the extraction of the precipitate signal from the matrix contribution and other contributions, such as from the sample surfaces and carbon contamination. This is a digital equivalent of the long-established extraction replica technique with the major advantages of

- Not involving chemical alteration of the sample and the possible alteration of the outer layers of the precipitates.
- Not losing their connection to the micro/nano-structure of the sample.

Our method includes the correction of a variety of systematic effects, including some arising from the non-idealities of the spectrometer and the microscope, as well as making full use of principal component analysis to separate the real signals from noise contributions. Of particular note is the role of EXELFS in perturbing the background shape and the minimisation of this effect by the processing used. The procedures developed have huge benefits for the quantitative analysis of the size and chemistry of the precipitates, since this will be much easier to perform on the extracted spectrum images than on the raw data containing additional matrix and other contributions. Our forthcoming companion paper to this publication will discuss the detailed quantification of the precipitates in such digitally extracted spectrum images in detail.

Acknowledgements

We are grateful to the European Commission for funding this work via the Research Fund for Coal and Steel (Precipitation in High Manganese Steels, RFSR-CT-2010-00018). The majority of the samples used in this work were provided by ThyssenKrupp Steel Europe AG and we are particularly thankful to Dr Georg Paul for his support and the provision of the samples. We are also grateful to the other partners (Dr Ian Zuazo, Arcelor Mittal Maizieres Research (AMMR), Metz; Dr Beatriz Lopez, Centro de Estudios e Investigaciones Técnicas de Guipúzcoa (CEIT), San Sebastian; Prof. David Porter, University of Oulu (UO), Oulu; Prof. Malin Selleby, Kungliga Tekniska Högskolan (KTH), Stockholm; Dr Bengt Hallstedt, RWTH Aachen University (RWTH), Aachen) for sharing

unpublished data on steel nanoprecipitation and thermodynamic modelling which informed our discussions. This work was only possible because of the generous provision of the MagTEM facility by SUPA and the University of Glasgow. We would like to thank Paul Thomas and Bernhard Schaffer of Gatan for their help with the scripting and their advice and help on the use of Digital Micrograph.

References

- [1] R.M. Fisher, Extraction replica technique for electron metallography, *J. Appl. Phys.* 24 (1953) (113–113).
- [2] I. Uchiyama, A. Fukami, S. Katagiri, Observation of precipitates and inclusions in steel by extraction replica technique, *J. Electron Microsc.* 5 (1957) 28–33.
- [3] A.J. Craven, M. MacKenzie, A. Cerezo, T. Godfrey, P.H. Clifton, Spectrum imaging and three-dimensional atom probe studies of fine particles in a vanadium micro-alloyed steel, *Mater. Sci. Tech.* 24 (2008) 641–650.
- [4] A.V. Khvan, B. Hallstedt, Thermodynamic description of the Fe–Mn–Nb–C system, *Calphad* 39 (2012) 62–69.
- [5] D. Blavette, F. Vurpillot, B. Deconihout, A. Menand, Tomography Atom Probe 3D Imaging at the Atomic Level, in: F.A. Lasagni, A.F. Lasagni (Eds.), *Fabrication and Characterization in the Micro-Nano Range: New Trends for Two and Three Dimensional Structures*, Springer-Verlag, Berlin, Berlin, 2011, pp. 201–222.
- [6] M. MacKenzie, A.J. Craven, C.L. Collins, Nanoanalysis of very fine VN precipitates in steel, *Scr. Mater.* 54 (2006) 1–5.
- [7] J. Scott, P.J. Thomas, M. MacKenzie, S. McFadzean, J. Wilbrink, A.J. Craven, W.A. P. Nicholson, Near-simultaneous dual energy range EELS spectrum imaging, *Ultramicroscopy* 108 (2008) 1586–1594.
- [8] A. Gubbens, M. Barfels, C. Trevor, R. Twisten, P. Mooney, P. Thomas, N. Menon, B. Kraus, C. Mao, B. McGinn, The GIF Quantum, a next generation post-column imaging energy filter, *Ultramicroscopy* 110 (2010) 962–970.
- [9] T. Malis, S.C. Cheng, R.F. Egerton, EELS Log-ratio technique for specimen-thickness measurement in the TEM, *J. Electron Microsc. Tech.* 8 (1988) 193–200.
- [10] K. Iakoubovskii, K. Mitsuishi, Y. Nakayama, K. Furuya, Thickness measurements with electron energy loss spectroscopy, *Microsc. Res. Tech.* 71 (2008) 626–631.
- [11] M. Bosman, M. Watanabe, D.T.L. Alexander, V.J. Keast, Mapping chemical and bonding information using multivariate analysis of electron energy-loss spectrum images, *Ultramicroscopy* 106 (2006) 1024–1032.
- [12] R.F. Egerton, *Electron Energy-Loss Spectroscopy in the Electron Microscope*, Springer, New York, 2011.
- [13] M. Schaffer, B. Schaffer, Q. Ramasse, Sample preparation for atomic-resolution STEM at low voltages by FIB, *Ultramicroscopy* 114 (2012) 62–71.
- [14] <http://hyperspy.org>.
- [15] G. Lucas, P. Burdet, M. Cantoni, C. Hebert, Multivariate statistical analysis as a tool for the segmentation of 3D spectral data, *Micron* (52–53) (2013) 49–56.
- [16] J.A. Wilson, A.J. Craven, Improving the analysis of small precipitates in HSLA steels using a plasma cleaner and ELNES, *Ultramicroscopy* 94 (2003) 197–207.
- [17] A.J. Craven, L.A.J. Garvie, Electron-energy-loss near-edge structure (ELNES) on the carbon K-edge in transition-metal carbides with the rock-salt structure, *Microsc. Microanal. Microstruct.* 6 (1995) 89–98.
- [18] A.J. Craven, The electron energy-loss near-edge structure (ELNES) on the N K-edges from the transition metal mononitrides with the rock-salt structure and its comparison with that on the C K-edges from the corresponding transition metal monocarbides, *J. Microsc.-Oxf.* 180 (1995) 250–262.
- [19] D.E. Gai, V.I. Grebennikov, O.R. Bakieva, D.V. Surnin, A.N. Deev, Spectroscopy of extended electron energy loss fine structures for quantitative analysis of the local atomic structure in ultrathin oxide films on the surface of 3D-metals, *J. Struct. Chem.* 49 (2008) S174–S189.
- [20] A.J. Craven, K. He, L.A.J. Garvie, T.N. Baker, Complex heterogeneous precipitation in titanium-niobium microalloyed Al-killed HSLA steels - I. (Ti,Nb) (C,N) particles, *Acta Mater.* 48 (2000) 3857–3868.
- [21] H.J. Goldschmidt, *Interstitial Alloys*, Butterworths, London, 1957.